Energy Storage Materials 27 (2020) 117–123

Contents lists available at ScienceDirect

Energy Storage Materials

journal homepage: www.elsevier.com/locate/ensm

Dual-functional interfaces for highly stable Ni-rich layered cathodes in sulfide all-solid-state batteries

Sixu Deng [a,1], Xia Li [a,1], Zhouhong Ren [b,1], Weihan Li [a], Jing Luo [a], Jianwen Liang [a], Jianneng Liang [a], Mohammad Norouzi Banis [a], Minsi Li [a], Yang Zhao [a], Xiaona Li [a], Changhong Wang [a], Yipeng Sun [a], Qian Sun [a], Ruying Li [a], Yongfeng Hu [c], Huan Huang [e], Li Zhang [d], Shigang Lu [d], Jun Luo [b,**], Xueliang Sun [a,*]

[a] Department of Mechanical and Materials Engineering, University of Western Ontario, London, Ontario, N6A 5B9, Canada
[b] Center for Electron Microscopy and Tianjin Key Lab of Advanced Functional Porous Materials, Institute for New Energy Materials and Low-Carbon Technologies, School of Materials Science and Engineering, Tianjin University of Technology, Tianjin, 300384, China
[c] Canadian Light Source, 44 Innovation Boulevard, Saskatoon, Saskatchewan, S7N 2V3, Canada
[d] China Automotive Battery Research Institute Co. Ltd, Fifth Floor, No. 43, Mining Building, North Sanhuan Middle Road, Beijing, 100088, China
[e] Glabat Solid-State Battery Inc., 700 Collip Circle, London, Ontario, N6G 4X8, Canada

ARTICLE INFO

Keywords:
Ni-rich NMC cathodes
Sulfide electrolytes
Li_3PO_4 modification
Side-reactions
Microstructural cracks

ABSTRACT

All-solid-state lithium-ion batteries (ASSLIBs) are expected as safe and high-performance alternatives to replace the conventional liquid-based lithium-ion batteries. However, the incompatible interface between the most cathode materials and sulfide-based solid electrolytes is still challenging the stable delivery of electrochemical performance for ASSLIBs. Herein, a dual-functional Li_3PO_4 (LPO) modification is designed for Ni-rich layered oxide cathodes in sulfide-based ASSLIBs to realize the high performance. The modified cathode demonstrates a significantly improved initial capacity of 170.6 mAh g^{-1} at 0.1C, better rate capability, and reduced polarization compared to the bare cathode. More importantly, a stable long-term cycling is achieved with a low capacity degradation rate of 0.22 mAh g^{-1} per cycle for 300 cycles at 0.2C. The detailed surface chemical and structural evolutions are studied via X-ray absorption near edge spectroscopy, X-ray photoelectron spectroscopy, and transmission electron microscopy. The results indicate that the LPO modification not only significantly suppresses the side-reactions with sulfide electrolyte but also helps to alleviate the deterioration of the microstructural cracks during the electrochemical reactions. This work provides an ideal and controllable interfacial design for realizing high performance sulfide-based ASSLIBs, which is readily applicable to other solid-state battery systems.

1. Introduction

Along with the rapid development of electric vehicles (EVs), the safety concerns and insufficient energy density of conventional lithium-ion batteries with the use of liquid organic electrolytes have become urgent challenges to be solved [1,2]. All-solid-state lithium-ion batteries (ASSLIBs) are expected to be a promising alternative considering the use of non-flammable inorganic solid electrolytes and the potential boost of energy density due to a simplified battery structure [3,4]. Among the developed solid-state electrolytes, sulfide-based electrolytes, providing high Li^+ conductivities of 10^{-2}-10^{-4} S cm^{-1} at room temperature, show great promise to replace the commercial liquid electrolytes [5,6]. However, the application of sulfide-based electrolytes in ASSLIBs still has several outstanding challenges and the cycling performance of the reported batteries decays dramatically with the low initial capacity and Columbic efficiency [7].

Interfacial incompatibility between cathode materials and sulfide-based electrolytes is the first challenge to the performance of ASSLIBs. The interfacial issues of cathodes mainly derive from the instability of the electrolytes at high voltages, leading to severe side-reactions with cathodes such as the formation of unfavorable cathode electrolyte interface (CEI) and degradation of the surficial structure of cathodes [8]. As a

* Corresponding author.
** Corresponding author.
E-mail addresses: jluo@tjut.edu.cn (J. Luo), xsun@eng.uwo.ca (X. Sun).
[1] The authors contribute equally to this work.

https://doi.org/10.1016/j.ensm.2020.01.009
Received 13 October 2019; Received in revised form 22 December 2019; Accepted 9 January 2020
Available online 13 January 2020

result, the cycling performance decays dramatically with the low initial capacity and Columbic efficiency [9]. As reported in many previous studies, coatings are the most effective strategies to alleviate the side-reactions, such as using $LiNbO_3$, $LiAlO_2$, $Li_4Ti_5O_{12}$, etc. [10–12] Another severe challenge is the integration of high capacity cathodes with outstanding volume change in ASSLIBs. Ni-rich $LiNi_xMn_yCo_{1-x-y}O_2$ (NMC) layered oxide cathodes are capable of delivering high discharge capacity greater than 200 mAh g^{-1}, especially with the high Ni content ($x \geq 0.8$) [13–15]. However, due to the anisotropic volume change induced by the unstable Ni^{4+} species in Ni-rich NMC during charging and discharging, Ni-rich NMC in the sulfide-based ASSLIBs still suffers from the severe contact loss between cathode particles and sulfide electrolytes [16,17]. The irreversible volume change of cathodes leads to the internal microstructural cracks emerge and propagate along the grain boundaries from the bulk to surface [18,19], therefore, block the Li^+ diffusion not only inside the secondary particles of cathodes but also at the interface between cathode particles and sulfide electrolytes [20,21]. As a result, the obvious capacity loss can be detected during the cycling. It is worth noting that although various surficial coating materials have been reported to alleviate side-reactions between sulfide SSEs and cathode materials, very few studies gave effort to address the challenge of microstructural cracks and contact loss derived by cathode volume change.

To overcome the two challenges at cathode part in sulfide-based ASSLIBs, in this work, we construct a dual-functional hierarchical Li_3PO_4 (LPO) modification via atomic layer deposition (ALD) for Ni-rich NMC ($LiNi_{0.8}Mn_{0.1}Co_{0.1}O_2$, in short HLPO@NMC811) cathodes in sulfide-based ASSLIBs. In our previous study, an ALD LPO solid electrolyte was adopted as the interfacial materials to tailor the grain boundaries of Ni-rich NMC cathodes [22]. The infused LPO not only eliminated interfacial reactions with the liquid electrolyte at the grain boundaries, but also alleviated the microstructural cracks and phase evolution from layer to spinel structure, which significantly improved the cycling stability of Ni-rich NMC cathodes in liquid electrolytes. To impart and further advance this developed structure in ASSLIBs, in this research, we first infuse a primary LPO coating layer of 10-nm thick into the inner of NMC811 particles and then deposit a secondary LPO coating layer to shield the NMC811 surface. Detailed electrochemical and material characterizations demonstrate that the dual-functional modification by hierarchical LPO not only effectively alleviates the severe side-reactions with sulfide electrolyte ($Li_{10}GeP_2S_{12}$, in short LGPS) but also suppresses the microstructural cracks of cathodes during charge/discharge cycling, significantly improves the cycling stability of Ni-rich NMC cathodes in sulfide-based ASSLIBs. Our dual-functional modification design shed lights on simultaneously solving the two key challenges of Ni-rich layered oxide cathodes for sulfide-based ASSLIBs and present promising ultra-long cycle life over 300 cycles of sulfide-based ASSLIBs.

2. Material and methods

2.1. Preparation of ALD LPO modified NMC811 cathodes

The lithium phosphate (LPO) was deposited on the surface of NMC811 powders using lithium tertbutoxide (LiOtBu) and trimethyl phosphate (TMPO) as precursors in a Savannah 100 ALD system (Cambridge Nanotech, USA). The source temperatures for LiOtBu and TMPO were 180 °C and 75 °C, respectively. The deposition temperature for LPO was 250 °C. During one ALD cycle, LiOtBu and TMPO were alternatively introduced into the reaction chamber with a pulse time of 2 s, and the pulsing of each precursor was separated by a 15 s purge with N_2. The primary LPO coating layer with a thickness of 10 nm was deposited on the surface of NMC811 powders by ALD. For infusion, the LPO-coated cathode powder were further annealed at 600 °C for 2 h. Furthermore, the LPO-annealed powders were subject to another ALD LPO coating with the thickness of 1 nm, 5 nm, or 10 nm.

2.2. Characterizations

X-ray power diffraction (XRD) measurements were carried out on a Bruker D8 Advance Diffractometer (Cu-Ka source, 40 kV, 40 mA). The morphologies of various cathodes were captured using field emission scanning electron microscopy (FESEM, Hitachi S4800) and high-resolution transmission electron microscopy (HRTEM, JEOL 2010FEG). The morphology and microstructure of cycled NMC811 cathodes were obtained by focused ion beam (FIB, Helios NanoLab 460HP, FEI)/FESEM (FE-SEM; JEOL JSM-7001F) for a detailed structural analysis. The obtained FIB samples were further investigated by aberration-corrected scanning transmission electron microscopy (STEM, Titan Cubed Themis G2 300) with elemental mapping images. To avoid contamination of samples, the cycled samples were scratched from the pallet and sealed in a glovebox under Ar. After that, the sealed samples were quickly transferred to the corresponding techniques for further measurements. The X-ray photoelectron spectroscopy (XPS) were measured with a monochromatic Al Kα source (1486.6 eV) in a Kratos AXIS Nova Spectrometer. The Ar filled glovebox was connected with XPS machine to avoid the exposure of air. X-ray absorption near edge structure (XANES) measurements were carried out at the Canadian Light Source (CLS). S, P, Ni, Co, and Mn K-edge XANES were collected using fluorescence yield mode on the soft X-ray microcharacterization beamline (SXRMB). To avoid air exposure, all the samples were covered with Mylar film in glovebox under Ar, and then transferred to the chamber of the corresponding beamline.

2.3. Electrochemical testing

The fabrication of all-solid-state batteries was carried out in an Ar-filled glovebox. Firstly, the electrolyte layer was prepared by pressing 70 mg commercial $Li_{10}GeP_2S_{12}$ (LGPS, 99.95%, MSE supplies, LLC) at 2 ton (~250 MPa) to form a pellet with 10 mm diameter. The cathode composite was then mixed with NMC811 cathodes powder and commercial LGPS powder at a weight ratio of 70:30.10 mg as-prepared cathode composite was spread on the surface of LGPS electrolyte followed by pressing at 3 ton (~380 MPa). Finally, a piece of In foil (99.99%, Φ 10 mm, thickness 0.1 mm) was put onto the other side of the LGPS pellets with a Cu foil and pressed at 0.5 ton (~65 MPa). The three-layered pellet (cathode composite/LGPS/In anode) was sandwiched between two stainless-steel rods as current collectors for both positive and negative electrodes. No extra pressure was applied on the final tested all-solid-state batteries. The galvanostatic charge/discharge characteristics were tested in a range of 2.7-4.5 V vs. Li/Li^+, at room temperature by using a multichannel battery tester (LAND CT-2001A, Wuhan Rambo Testing Equipment Co., Ltd.). Cyclic voltammograms (CV) were collected on a versatile multichannel potentiostation 3/Z (VMP3) using a scan rate of 0.05 mV s^{-1} between 2.7-4.5 V vs. Li/Li^+. Electrochemical impedance spectroscopy (EIS) was also performed on the versatile multichannel potentiostat 3/Z (VMP3) by applying an AC voltage of 10 mV amplitude in the 7000 kHz to 100 mHz frequency range.

3. Results and discussion

For comparison, four types of NMC811 cathodes with different modification procedures (Fig. S1) were prepared, including (i) bare NMC811, (ii) only a primary ALD LPO coating on NMC811 (LPO@NMC811), (iii) infused LPO into NMC811 by subsequent annealing (iLPO@NMC811), and (iv) a secondary ALD LPO coating on top of iLPO@NMC811 for a hierarchical coverage (HLPO@NMC811). Fig. 1a schematically depicts the ultimate design of HLPO@NMC811. According to the scanning electron microscopy (SEM) and transmission electron microscopy (TEM) analyses, the conformal secondary LPO coating by ALD completely cover the cathode particle with a uniform thickness of 5 nm (Figure b–c and S2). The energy dispersive X-ray (EDX) elemental mappings of a cross-sectional HLPO@NMC811 particle cut by focused

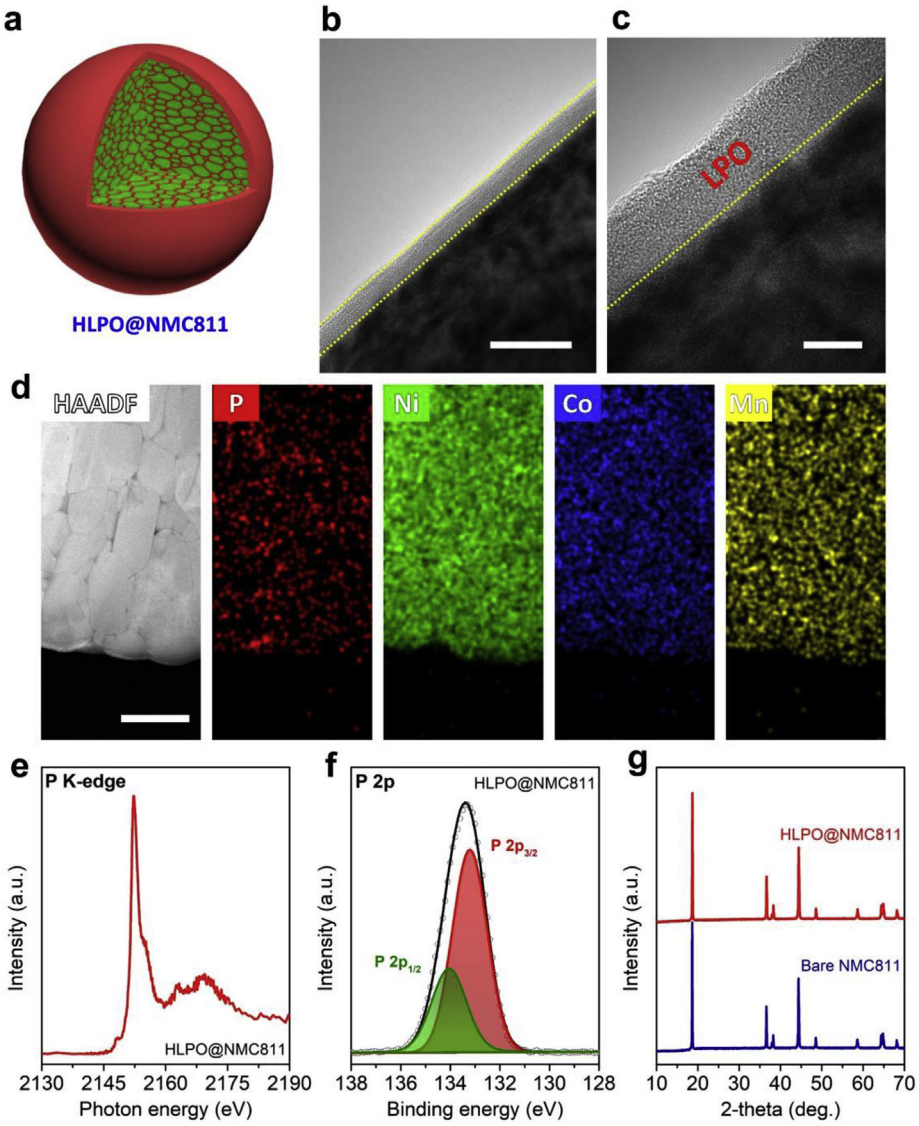

Fig. 1. Schematic structure and characterizations of HLPO@NMC811 modification. a) Schematic illustration of the detailed structure of HLPO@NMC811, b-c) HR-TEM images of the secondary LPO coating layer on the HLPO@NMC811 surface at different magnifications, d) EDX mappings of the cross-sectional HLPO@NMC811, e-f) P K-edge XANES and P 2p XPS spectra of HLPO@NMC811, g) XRD patterns of the bare NMC811 and HLPO@NMC811. Scale bars in (b), (c), and (d) are 20 nm, 5 nm, and 500 nm, respectively.

ion beam (FIB) are shown in Fig. 1d. The enriched P signals across the particle indicate the successful infusion of phosphorus element into the inner of cathode particles by annealing. The P K-edge X-ray absorption near edge structure (XANES) collected by the florescence yield (FLY) mode and P 2p X-ray photoelectron spectroscopy (XPS) analyses of HLPO@NMC811 confirm the chemistry of the LPO components (Fig. 1e and f). The FLY mode detects a depth up to several microns, obtaining information from the surfaces to the bulk of HLPO@NMC811 (considering the micron-sized scale of NMC811 secondary particles) [23]. The P signal can be detected in both P K-edge XANES and P 2p XPS spectra, indicating the LPO exists both on the surface and in the bulk structure of NMC811 particles. X-ray diffraction (XRD) patterns of the bare NMC811 and samples with different modifications show good retention of the NMC811 crystallinity without noticeable impurity phase caused by the ALD or annealing process (Fig. 1g and S3).

The bare NMC811, LPO@NMC811, iLPO@NMC811, and HLPO@NMC811 were respectively mixed with the LGPS electrolytes as a composite cathode layer for electrochemical evaluations in ASSLIBs. The detailed fabrication process of the ASSLIBs is described in the experimental section. Fig. 2a compares the first-cycle charge/discharge curves of these four different ASSLIBs at 0.1C. The initial discharge capacity of the bare cathode is only 96.4 mAh g^{-1} with the severe polarization. Compared to the bare cathode, all LPO modified cathodes exhibit the obviously improved discharge capacities, with the HLPO@NMC811 cathode demonstrating the most significant improvement. The HLPO@NMC811 based ASSLIB achieves a high discharge capacity of 170.6 mAh g^{-1} with the smallest polarization. Upon further cycling at 0.1C, the ASSLIBs with different cathodes show dramatic difference in stability over 100 cycles (Fig. 2b). The ASSLIB using bare NMC811 is completely failed within 50 cycles. On sharp contrast, the HLPO@NMC811 based ASSLIB maintains a high discharge capacity of 133.0 mAh g^{-1} after 100 cycles, which still far surpasses even the initial discharge capacity of the cells using bare NMC811 and LPO@NMC811. As shown in Fig. S4, the optimized thickness of the secondary ALD LPO coating for HLPO@NMC811 is 5 nm. An unoptimized secondary coating could be too thin to prevent side-reactions with the sulfide electrolyte or too thick that in turn limit the ASSLIB performance due to additional internal resistance. In this context, ALD is a unique technique that controls coating precision to the nanoscale [24]. Moreover, the superiority of the HLPO@NMC811 cathode over other NMC811 based cathodes is also consistently exhibited in terms of high Coulombic efficiency and low internal resistance during cycling. The HLPO@NMC811 based ASSLIB possesses a significantly increased initial Coulombic efficiency of 75.1% (versus 64.9% of the bare NMC811 cell) and maintains a high Coulombic efficiency above 99% during the following cycles (Fig. 2c). As shown in Fig. 2d, the HLPO@NMC811 based ASSLIB shows the smallest internal

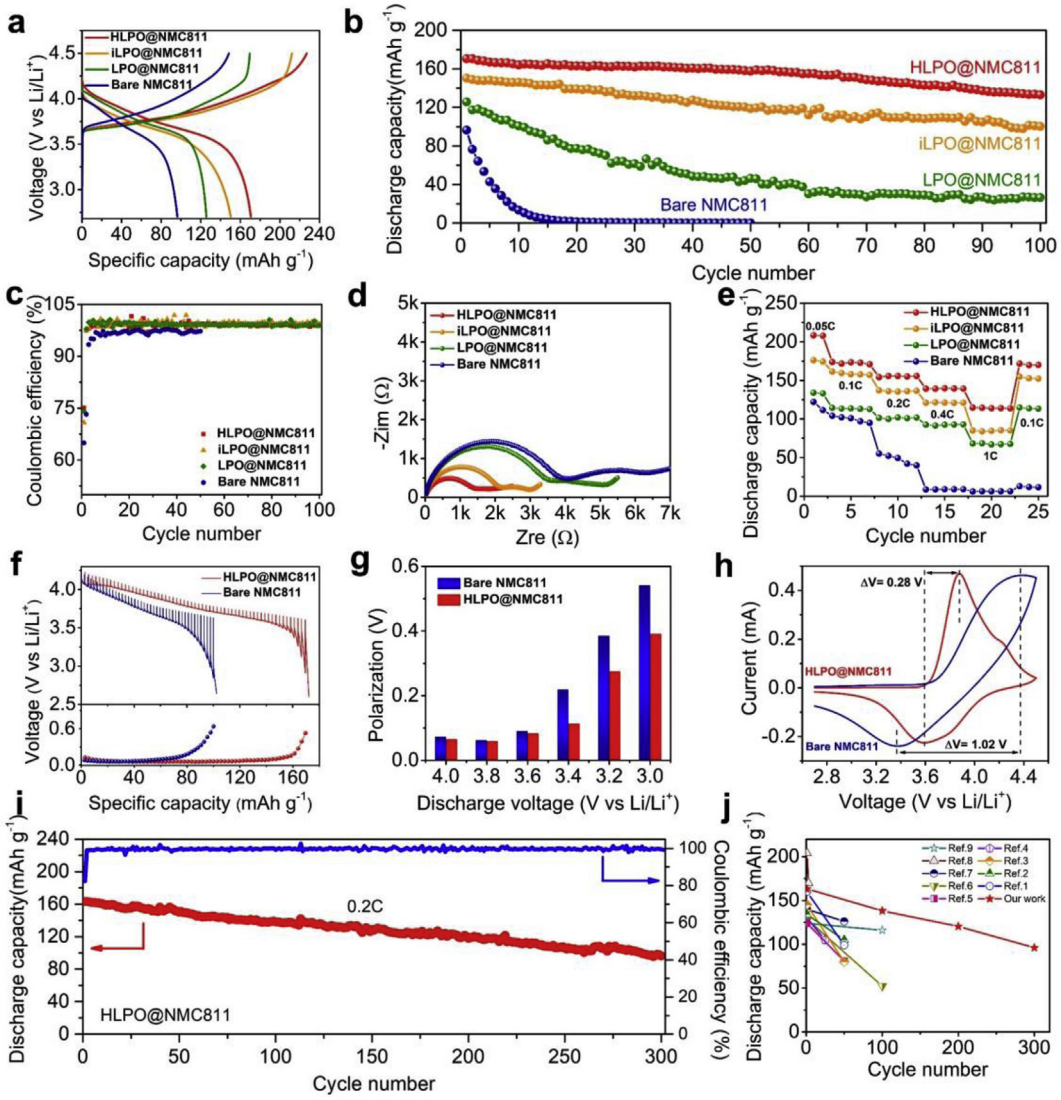

Fig. 2. Effectiveness of various LPO modifications for ASSLIBs performance. a) Charge/discharge curves of the first cycle, b) cycling stabilities at 0.1C, c) corresponding Coulombic efficiencies, d) EIS plots after 100 cycles, and e) rate capability for the four types of NMC811 cathodes. More details of the optimal HLPO@NMC811 cathode in comparison with the bare NMC811 regarding f) GITT curves during the discharge process (top) and corresponding polarization plots (bottom), g) polarization plots at selected discharge voltages, h) CV profiles at the first cycle. i) Long-term cycling stability of the HLPO@NMC811 cathode at 0.2C. j) Cycling performance of our work and reported Ni-rich NMC cathodes in sulfide-based ASSLIBs.

resistance after 100 cycles by up to several folds among all the cells, even though the HLPO@NMC811 cathode experienced the greatest depths of charge and discharge.

Interestingly, despite the inferior performance to the HLPO@NMC811 based ASSLIB, the iLPO@NMC811 cathode delivers higher discharge capacity, more stable cycling performance, and much lower internal resistance than the LPO@NMC811. This suggests that the cracking induced contact loss between cathode particles and the sulfide electrolyte has a more serious influence on the electrochemical performance than the interfacial side-reactions. The electrochemical impedance spectroscopy (EIS) plots show a consistent trend. More specifically, the EIS plots of the ASSLIBs using different NMC811 cathodes show only one semicircle before cycling, which corresponded to the bulk resistance of the solid electrolyte (Fig. S5) [20]. After cycling, two semicircles emerge in the high and medium frequencies, indicating deteriorative side-reactions and/or loss of contact at the interface between NMC811 and LGPS during cycling. The substantially larger impedance of the LPO@NMC811 cell than that of the iLPO@NMC811 cell again confirms the cracking induced battery degradation. The corresponding equivalent circuit for fitting the EIS plots and the fitted resistance values are shown in Fig. S6 and Table S1, respectively.

Under a wide range of current densities from 0.05C to 1C, the ASSLIB using HLPO@NMC811 cathode demonstrates the most outstanding rate capability over other NMC811 based cathodes (Fig. 2e). Even at 1C, the HLPO@NMC811 cathode still delivered the discharge capacity of about 115 mAh g^{-1}. However, the discharge capacity of the bare cathode dropped to less than 10 mAh g^{-1} at the same current density. Correspondingly, the charge/discharge voltage profiles of the HLPO@NMC811 based ASSLIB exhibit reduced polarization compared to that of the bare NMC811 cell at all current densities (shown in Fig. S7). Furthermore, the galvanostatic intermittent titration technique (GITT) curves of the bare NMC811 and HLPO@NCM811 cathodes during the discharge process are given in Fig. 2f along with the corresponding polarization plots at different voltages in Fig. 2g. Obviously, HLPO@NCM811 cathode presents smaller polarization potential than that of the bare NMC811 cathode at each voltage, indicating effective stabilization of the cathode throughout the discharging process by the hierarchical LPO modification. Cyclic voltammetry (CV) profiles of the

bare and LPO modified cathodes are shown in Fig. 2h and S8-9. The voltage gap between the redox peaks of the HLPO@NCM811 cathode is significantly smaller than that of the bare NMC811 cathode. Meanwhile, the HLPO@NCM811 cathode shows a much lower current value at the cut-off charging voltage of 4.5 V than the bare NMC811 cathode, indicating substantially reduced oxidized reaction with sulfide electrolyte. Fig. 2i shows stable long-term cycling of the HLPO@NCM811 based ASSLIB at 0.2C for 300 cycles. The modified cathode demonstrates a high initial discharge capacity of 163.2 mAh g^{-1} and retains 96.1 mAh g^{-1} after 300 cycles. The average capacity decay is 0.22 mAh g^{-1} per cycle, which is a great improvement for sulfide based ASSLIBs. Fig. 3j compares the cycling performance between HLPO@NMC811 and the reported Ni-rich NMC in sulfide-based ASSLIBs. The sources of the data are listed in Table S2. It is apparent that the ultra-long cycling stability of the LPO modified cathode overtakes previous results. Overall, the HLPO@NMC811 cathode with hierarchical LPO modification promotes higher specific capacity, improved cycling stability, enhanced rate capability, and reduced voltage polarizations compared to the bare NMC811 cathode, which thanks to the effective suppressions in side-reactions with sulfide electrolyte and internal cracks of NMC811 during the electrochemical cycling.

In order to investigate the interfacial chemical evolution as well as the protective role of the LPO modification, XPS and XANES are performed. Fig. 3b–c and S10 show the XPS results of the LGPS electrolytes collected from the cycled composite electrodes using bare NMC811 and HLPO@NMC811. The XPS spectra of pristine LGPS are provided as references. From S 2p XPS spectra, in addition to the pristine LGPS features at 161.2 eV, the decomposed byproducts of LGPS are observed at 160.1 eV and 162.9 eV from both electrodes because of the inevitable decomposition of LGPS at high voltages [25], with the bare NMC811 electrode shows higher relative content of Li_2S side product. While the LGPS from both electrodes share common self-decomposition products of Li_2S and -S-S- [26–28], the dramatically different occurrence of SO_3^{2-} and SO_4^{2-} species indicates different degrees of electrolyte oxidation caused by the cathodes. Presumably, the oxidation of LGPS comes across oxygen participation from the NMC811 structure. Upon increasing depth of charge, the side-reactions between NMC811 and electrolyte become more serious, which lead to the evolution of the layer structure on the cathode particle surface [29]. The structural change is usually accompanied with increase in the effective electron density of oxygen, resulting in the formation of oxygen vacancies [30–32]. The evolution of cathode in turn accelerates the oxidation of electrolyte and the formation of CEI layer, therefore damaging the cycling stability of cathode as shown in Fig. 2b. The high relative peak intensities of SO_3^{2-} and SO_4^{2-} in Fig. 3b suggest severe reactions between the unprotected NMC811 and LGPS. Impressively, the SO_4^{2-} signals are essentially absent with only a small amount of SO_3^{2-} when

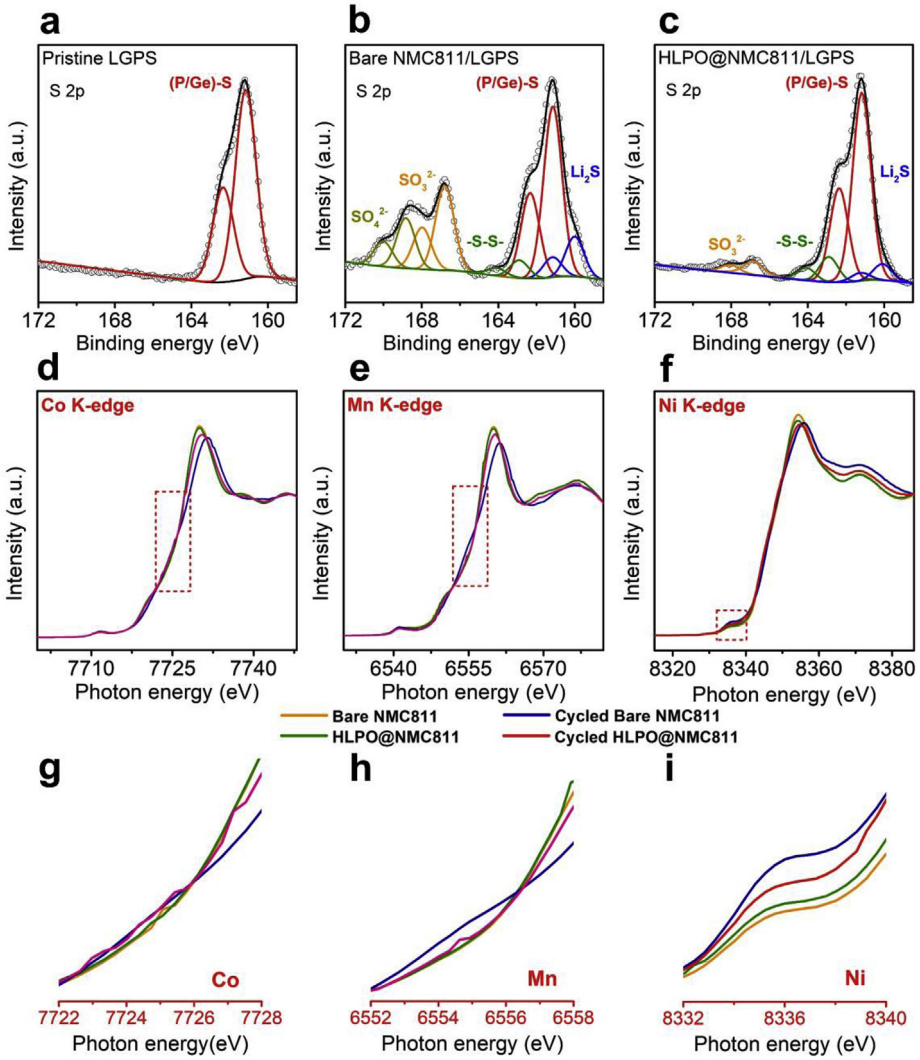

Fig. 3. Understanding the interfacial chemical evolution during electrochemical reactions. S 2p XPS spectra of the a) pristine LGPS, b) bare NMC811/LGPS electrode after cycling, and c) HLPO@NMC811/LGPS electrode after cycling. d-i) Co, Mn, Ni K-edge XANES spectra of the bare NMC811 and HLPO@NMC811 electrodes before and after cycling: d, g) Co K-edge, e, h) Mn K-edge, f, i) Ni K-edge.

using the HLPO@NMC811, proving effective suppression of side-reactions by the LPO modification. Similar conclusion can be reached from the P 2p and Ge 3d XPS spectra comparisons (Fig. S10). After cycling, the characteristic PS_4^{3-} spin-orbit doublet of LGPS is hardly observable on the P 2p spectrum of the bare NMC811 electrode, while the $P_2S_6^{2-}$ peaks (peak B) become stronger. At the same time, three new phosphorus species are found (i.e., C, D, and E), which may be attributed to the -P-S-P- or -Ge-S-P- bonds [33]. As the Ge 3d spectra shown in Fig. S10b, the new oxidized species in bare NMC811 electrode are also detected. In great contrast, the evolution of both phosphorus and germanium elements after cycling is effectively suppressed by the hierarchical LPO modification. The S and P XANES spectra for the bare NMC811 and HLPO@NMC811 electrodes are compared in Fig. S11 and show high consistency with the XPS results. Comparing the S K-edge XANES (Fig. S11a), the intensity of the peak at 2481.9 eV increases dramatically for the bare NMC811 electrode, confirming the formation of SO_x from the severe side-reactions between NMC811 and LGPS during cycling [34,35]. On the contrary, the HLPO@NMC811 shows alleviated side-reactions with electrolyte, therefore effectively suppress the formation of SO_x. The S and P XANES spectra of LPO@NMC811 and iLPO@NMC811 are shown in Fig. S12 to further demonstrate the different levels of alleviation in the different LPO modification.

The K-edge XANES spectra of transition metals (TMs, including Co, Mn, and Ni) are exhibited in Fig. 3d–i and S13-14 to understand the structural evolution of the layered NMC811 during cycling. Generally, the oxidation states of TMs in layered cathodes are highly related to the threshold energy position in the K-edge XANES spectra, while the local structural environment between TMs and oxide is determined by the shape of the peaks [36]. Before cycling, both the energy position and the shape of peaks of TMs K-edge XANES spectra of the HLPO@NMC811 cathode show no obvious difference to the bare NMC811 cathode, suggesting the unchanged chemical environments of the TMs upon LPO modification. Interestingly, both Co and Mn K-edge XANES spectra for the cycled bare NMC811 cathode show spectral shape variations without energy shift, indicating changes of local environment of Co and Mn atoms after cycling [15,37]. In contrast, the shape changes of the spectra for the cycled HLPO@NMC811 cathode are less prominent. Meanwhile, the increased intensity of pre-edge peak for Ni K-edge at 8336.0 eV can be observed in the spectra for both cycled bare NMC811 and HLPO@NMC811 cathodes, indicating local structure distortion of Ni atoms after cycling [38]. However, the HLPO@NMC811 shows much lower level of distortion than the bare NMC811 cathode. Therefore, the obvious shape variations of Co, Mn K-edge spectra and intensity increasing of Ni K-edge spectra after cycling demonstrate that severe side-reactions with LGPS lead to surficial structure evolution of cathode for the cycled bare NMC811, while can be effectively alleviated by the hierarchical LPO modification.

The microstructural evolution of Ni-rich NMC cathodes during the electrochemical reactions is another important factor that determines the performance in sulfide-based ASSLIBs. Fig. 4 compares the cross-sectional TEM images and EDX mappings of the bare NMC811 and HLPO@NMC811 cathode particles after cycling. Obvious microstructural cracks can be observed in the bare NMC811 particle and deteriorate from central to surface, which can be ascribed to the anisotropic lattice variation induced micro-strain along the grain boundaries of primary cathode particles [39]. As a result, the cracks between primary particles seriously block the lithium ion and electron transfer, therefore isolated primary particles were no longer active in the following cycles, leading to the dramatic performance degradation. On the contrary, the HLPO@NMC811 particle maintains its original microstructure without obvious cracks (Fig. 4c). As confirmed by the EDX mapping results,

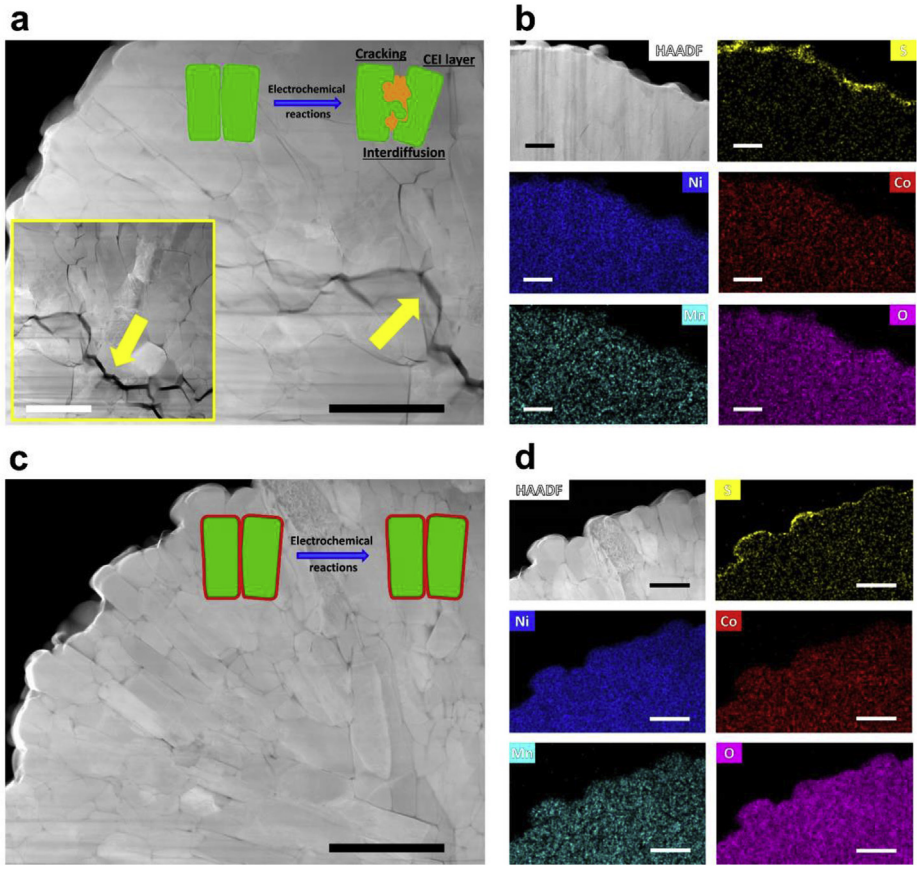

Fig. 4. Understanding the microstructural evolution of NMC811 during electrochemical reactions. a) Cross-sectional FIB-TEM images of the cycled bare NMC811 particle and b) corresponding EDX mappings. c) Cross-sectional FIB-TEM images of the cycled HLPO@NMC811 particle and corresponding EDX mappings. Scale bars are 1 μm (a and c) and 500 nm (b and d).

despite the uniform distribution of Ni, Mn, Co, and O elements in the bulk of NMC811, the obviously different distributions of S signals are observed for the bare NMC811 and the HLPO@NMC811. The accumulation of sulfur element on the particle surface is much thicker for the bare NMC811 particle than the HLPO@NMC811, indicating the tempting formation of unfavorable CEI layer due to the severe side-reactions with sulfide electrolyte. On the contrary, the LPO modification effectively suppresses the side-reactions between NMC811 and sulfide electrolyte, therefore relieving the formation of CEI layer on the surface of cathode particles.

4. Conclusion

In conclusion, we demonstrate a dual-functional ALD LPO modification for Ni-rich NMC layered oxide cathodes for sulfide-based ASSLIBs. The local LPO lithium-ion conductor tailors not only the grain boundaries between the primary cathode particles but also the surface of the secondary particles. Microstructural and interfacial chemical/electrochemical stabilities are simultaneously addressed by the hierarchical design. The optimized HLPO@NMC811 cathode demonstrates significantly improved electrochemical performance with a high initial discharge capacity of 170.6 mAh g^{-1} at 0.1C, good rate capability, small voltage polarization, and encouraging capacity retention of 77.9% after 100 cycles at 0.1C. At a higher current density of 0.2C, a discharge capacity of 96.1 mAh g^{-1} is still maintained after 300 cycles. As confirmed by XPS and synchrotron XANES analyses, the severe side-reactions with LGPS and the surficial structure evolution of the bare NMC811 are effectively suppressed by the hierarchical LPO stabilization. The cross-sectional TEM studies combined with EDX mappings further reveal the microstructural stability of the HLPO@NMC811 cathode and the minimized interfacial electrolyte decomposition upon cycling, which is distinct from the cracked unprotected NMC811 particle with thick side-products on the surface. Our dual-functional modification design evidently addresses the two main issues of Ni-rich layered oxide cathodes at the same time for sulfide-based ASSLIBs, significantly improving the electrochemical performance, which is a key to the practical application of ASSLIBs in the near future.

Declaration of competing interest

The authors declare that they have no known competing financial interests or personal relationships that could have appeared to influence the work reported in this paper.

CRediT authorship contribution statement

Sixu Deng: Writing - original draft. **Xia Li:** Data curation. **Zhouhong Ren:** Data curation. **Weihan Li:** Data curation. **Jing Luo:** Writing - review & editing. **Jianwen Liang:** Data curation. **Jianneng Liang:** Data curation. **Mohammad Norouzi Banis:** Data curation. **Minsi Li:** Data curation. **Yang Zhao:** Data curation. **Xiaona Li:** Data curation. **Changhong Wang:** Data curation. **Yipeng Sun:** Data curation. **Qian Sun:** Methodology. **Ruying Li:** Methodology. **Yongfeng Hu:** Methodology. **Huan Huang:** Project administration. **Li Zhang:** Project administration. **Shigang Lu:** Project administration. **Jun Luo:** Supervision. **Xueliang Sun:** Supervision.

Acknowledgments

This work was supported by Natural Sciences and Engineering Research Council of Canada (NSERC), Canada Research Chair Program (CRC), Canada Foundation for Innovation (CFI), Ontario Research Fund (ORF), China Automotive Battery Research Institute Co., Ltd., Glabat Solid-State Battery Inc., Canada Light Source (CLS) at University of Saskatchewan, Interdisciplinary Development Initiatives (IDI) by Western University, University of Western Ontario, and the 111 project of China (D17003). Sixu Deng acknowledges support of a Mitacs Accelerate Fellowship. Xia Li acknowledges support of a Mitacs Elevate Postdoctoral Fellowship.

Appendix A. Supplementary data

Supplementary data to this article can be found online at https://doi.org/10.1016/j.ensm.2020.01.009.

References

[1] H. Li, Joule 3 (2019) 911–914.
[2] F. Lin, D. Nordlund, Y. Li, M.K. Quan, L. Cheng, T.-C. Weng, Y. Liu, H.L. Xin, M.M. Doeff, Nat. Energy 1 (2016) 15004.
[3] A. Manthiram, X. Yu, S. Wang, Nat. Rev. Mater. 2 (2017) 16103.
[4] W. Zhao, J. Yi, P. He, H. Zhou, Electrochem. Energy Rev. (2019), https://doi.org/10.1007/s41918-019-00048-0.
[5] N. Kamaya, K. Homma, Y. Yamakawa, M. Hirayama, R. Kanno, M. Yonemura, T. Kamiyama, Y. Kato, S. Hama, K. Kawamoto, A. Mitsui, Nat. Mater. 10 (2011) 682.
[6] P. Bron, S. Johansson, K. Zick, S. Dehnen, B. Roling, J. Schmedt auf der Günne, J. Am. Chem. Soc. 135 (2013) 15694–15697.
[7] A.M. Nolan, Y. Zhu, X. He, Q. Bai, Y. Mo, Joule 2 (2018) 2016–2046.
[8] W. Zhang, D.A. Weber, H. Weigand, T. Arlt, I. Manke, D. Schröder, R. Koerver, T. Leichtweiss, P. Hartmann, W.G. Zeier, J. Janek, ACS Appl. Mater. Interfaces 9 (2017) 17835–17845.
[9] F. Walther, R. Koerver, T. Fuchs, S. Ohno, J. Sann, M. Rohnke, W.G. Zeier, J. Janek, Chem. Mater. 31 (2019) 3745–3755.
[10] X. Li, M. Liang, J. Sheng, D. Song, H. Zhang, X. Shi, L. Zhang, Energy Storage Mater 18 (2019) 100–106.
[11] K. Okada, N. Machida, M. Naito, T. Shigematsu, S. Ito, S. Fujiki, M. Nakano, Y. Aihara, Solid State Ion. 255 (2014) 120–127.
[12] Y. Seino, T. Ota, K. Takada, J. Power Sources 196 (2011) 6488–6492.
[13] W. Liu, P. Oh, X. Liu, M.-J. Lee, W. Cho, S. Chae, Y. Kim, J. Cho, Angew. Chem. Int. Ed. 54 (2015) 4440–4457.
[14] H.-H. Ryu, K.-J. Park, C.S. Yoon, Y.-K. Sun, Chem. Mater. 30 (2018) 1155–1163.
[15] S. Guo, B. Yuan, H. Zhao, D. Hua, Y. Shen, C. Sun, T. Chen, W. Sun, J. Wu, B. Zheng, W. Zhang, S. Li, F. Huo, Nano Energy 58 (2019) 673–679.
[16] C.S. Yoon, D.-W. Jun, S.-T. Myung, Y.-K. Sun, ACS Energy Lett 2 (2017) 1150–1155.
[17] X. Xu, H. Huo, J. Jian, L. Wang, H. Zhu, S. Xu, X. He, G. Yin, C. Du, X. Sun, Adv. Energy Mater. 9 (2019) 1803963.
[18] U.-H. Kim, J.-H. Kim, J.-Y. Hwang, H.-H. Ryu, C.S. Yoon, Y.-K. Sun, Mater. Today 23 (2019) 26–36.
[19] K.-J. Park, H.-G. Jung, L.-Y. Kuo, P. Kaghazchi, C.S. Yoon, Y.-K. Sun, Adv. Energy Mater. 8 (2018) 1801202.
[20] R. Koerver, I. Aygün, T. Leichtweiß, C. Dietrich, W. Zhang, J.O. Binder, P. Hartmann, W.G. Zeier, J. Janek, Chem. Mater. 29 (2017) 5574–5582.
[21] R. Koerver, W. Zhang, L. de Biasi, S. Schweidler, A.O. Kondrakov, S. Kolling, T. Brezesinski, P. Hartmann, W.G. Zeier, J. Janek, Energy Environ. Sci. 11 (2018) 2142–2158.
[22] P. Yan, J. Zheng, J. Liu, B. Wang, X. Cheng, Y. Zhang, X. Sun, C. Wang, J.-G. Zhang, Nat. Energy 3 (2018) 600–605.
[23] A. Erbil, G.S. Cargill Iii, R. Frahm, R.F. Boehme, Phys. Rev. B 37 (1988) 2450–2464.
[24] X. Meng, X.-Q. Yang, X. Sun, Adv. Mater. 24 (2012) 3589–3615.
[25] Y. Zhu, X. He, Y. Mo, ACS Appl. Mater. Interfaces 7 (2015) 23685–23693.
[26] W. Zhang, F.H. Richter, S.P. Culver, T. Leichtweiss, J.G. Lozano, C. Dietrich, P.G. Bruce, W.G. Zeier, J. Janek, ACS Appl. Mater. Interfaces 10 (2018) 22226–22236.
[27] S. Wenzel, S. Randau, T. Leichtweiß, D.A. Weber, J. Sann, W.G. Zeier, J. Janek, Chem. Mater. 28 (2016) 2400–2407.
[28] X. Li, Z. Ren, M. Norouzi Banis, S. Deng, Y. Zhao, Q. Sun, C. Wang, X. Yang, W. Li, J. Liang, X. Li, Y. Sun, K. Adair, R. Li, Y. Hu, T.-K. Sham, H. Huang, L. Zhang, S. Lu, J. Luo, X. Sun, ACS Energy Lett 4 (2019) 2480–2488.
[29] P. Yan, J. Zheng, J.-G. Zhang, C. Wang, Nano Lett. 17 (2017) 3946–3951.
[30] S. Hwang, W. Chang, S.M. Kim, D. Su, D.H. Kim, J.Y. Lee, K.Y. Chung, E.A. Stach, Chem. Mater. 26 (2014) 1084–1092.
[31] J.D. Steiner, L. Mu, J. Walsh, M.M. Rahman, B. Zydlewski, F.M. Michel, H.L. Xin, D. Nordlund, F. Lin, ACS Appl. Mater. Interfaces 10 (2018) 23842–23850.
[32] C. Tian, D. Nordlund, H.L. Xin, Y. Xu, Y. Liu, D. Sokaras, F. Lin, M.M. Doeff, J. Electrochem. Soc. 165 (2018) A696–A704.
[33] W. Zhang, T. Leichtweiß, S.P. Culver, R. Koerver, D. Das, D.A. Weber, W.G. Zeier, J. Janek, ACS Appl. Mater. Interfaces 9 (2017) 35888–35896.
[34] N. Kornienko, J. Resasco, N. Becknell, C.-M. Jiang, Y.-S. Liu, K. Nie, X. Sun, J. Guo, S.R. Leone, P. Yang, J. Am. Chem. Soc. 137 (2015) 7448–7455.
[35] D.H. Kim, J.H. Kwak, J. Szanyi, S.J. Cho, C.H.F. Peden, J. Phys. Chem. C 112 (2008) 2981–2987.
[36] X. Yu, Y. Lyu, L. Gu, H. Wu, S.-M. Bak, Y. Zhou, K. Amine, S.N. Ehrlich, H. Li, K.-W. Nam, X.-Q. Yang, Adv. Energy Mater. 4 (2014) 1300950.
[37] E. Hu, X. Yu, R. Lin, X. Bi, J. Lu, S. Bak, K.-W. Nam, H.L. Xin, C. Jaye, D.A. Fischer, K. Amine, X.-Q. Yang, Nat. Energy 3 (2018) 690–698.
[38] P.-Y. Liao, J.-G. Duh, J.-F. Lee, J. Power Sources 189 (2009) 9–15.
[39] H. Kim, M.G. Kim, H.Y. Jeong, H. Nam, J. Cho, Nano Lett. 15 (2015) 2111–2119.